ADVANCED MATERIALS
www.advmat.de

Ultrafast Sub-100 fs All-Optical Modulation and Efficient Third-Harmonic Generation in Weyl Semimetal Niobium Phosphide Thin Films

Benjamin Tilmann, Avanindra Kumar Pandeya, Gustavo Grinblat, Leonardo de S. Menezes, Yi Li, Chandra Shekhar, Claudia Felser, Stuart S. P. Parkin, Amilcar Bedoya-Pinto,* and Stefan A. Maier*

Since their experimental discovery in 2015, Weyl semimetals have generated a large amount of attention due their intriguing physical properties that arise from their linear electron dispersion relation and topological surface states. In particular, in the field of nonlinear (NL) optics and light harvesting, Weyl semimetals have shown outstanding performances and achieved record NL conversion coefficients. In this context, the first steps toward Weyl semimetal nanophotonics are performed here by thoroughly characterizing the linear and NL optical behavior of epitaxially grown niobium phosphide (NbP) thin films, covering the visible to the near-infrared regime of the electromagnetic spectrum. Despite the measured high linear absorption, third-harmonic generation studies demonstrate high conversion efficiencies up to 10^{-4}% that can be attributed to the topological electron states at the surface of the material. Furthermore, nondegenerate pump–probe measurements with sub-10 fs pulses reveal a maximum modulation depth of ≈1%, completely decaying within 100 fs and therefore suggesting the possibility of developing all-optical switching devices based on NbP. Altogether, this work reveals the promising NL optical properties of Weyl semimetal thin films, which outperform bulk crystals of the same material, laying the grounds for nanoscale applications, enabled by top-down nanostructuring, such as light-harvesting, on-chip frequency conversion, and all-optical processing.

1. Introduction

In recent years, Weyl semimetals (WSMs) have attracted a large amount of attention in solid-state research. Their unique properties are determined by a single touching point of the conduction and valence bands in the electronic band structure, which features a linear electron dispersion.[1,2] In this so-called Weyl cone, electrons behave as massless, quasi-relativistic fermions and are described by the corresponding solution to the Dirac equation, the Weyl equation.[3] These Weyl nodes always appear in pairs of opposite chirality, separated in momentum space and connected by topologically protected surface states (Fermi arcs).[4,5] This peculiar electronic structure gives rise to material properties such as a high electron mobility,[6,7] low temperature superconductivity,[8–10] a huge magnetoresistance,[11,12] a strong anomalous Hall effect,[7,11,13] and the Adler–Bell–Jackiw anomaly.[14–17]

B. Tilmann, L. d. S. Menezes, S. A. Maier
Chair in Hybrid Nanosystems
Nanoinstitut München
Fakultät für Physik
Ludwig-Maximilians-Universität München
80539 München, Germany
E-mail: b.tilmann@physik.uni-muenchen.de

A. K. Pandeya, S. S. P. Parkin, A. Bedoya-Pinto
Max Planck-Institute of Microstructure Physics
Halle, 06120 Saale, Germany
E-mail: abedoya@mpi-halle.mpg.de

The ORCID identification number(s) for the author(s) of this article can be found under https://doi.org/10.1002/adma.202106733.

DOI: 10.1002/adma.202106733

G. Grinblat
Departamento de Física
FCEN
IFIBA-CONICET
Universidad de Buenos Aires
Buenos Aires C1428EGA, Argentina

L. d. S. Menezes
Departmento de Física
Universidade Federal de Pernambuco
Recife-PE 50670–901, Brazil

Y. Li
School of Microelectronics
MOE Engineering Research Center of Integrated Circuits for Next Generation Communications
Southern University of Science and Technology
Shenzhen 518055, China

C. Shekhar, C. Felser
Max Planck-Institute for Chemical Physics of Solids
01187 Dresden, Germany

Furthermore, the exceptional electronic properties of WSMs lead to outstanding optical properties that have been thoroughly investigated. It was shown that the second-order susceptibility of tantalum arsenide (TaAs) is two orders of magnitude larger than for high refractive index non-centrosymmetric dielectrics,[18] an efficient nonlinear (NL) photocurrent generation was also demonstrated,[19] the near infrared glass-coefficient was found to be the strongest so far reported[20] and efficient catalytic activity was observed for the hydrogen evolution reaction.[21] So far, experimental reports were limited to bulk[22,23] or micro structuring of the bulk crystal,[8,10,20] representing a natural restriction to the development of on-chip applications.

In this work, we investigate the linear and NL optical response of recently reported epitaxially grown thin films[24,25] of the prototypical type-I WSM niobium phosphide (NbP) and compare them to the performance of the bulk single crystal.[12] We determine the linear refractive index and extinction coefficient of NbP in the visible to near infrared regime by spectral ellipsometry and find them to be in reasonable agreement with theoretical predictions.[26] Third-harmonic generation (THG) and ultrafast non-degenerate pump–probe spectroscopy are used to measure the nonlinear optical response and electronic dynamics with sub-10 fs resolution. We show that the thin film reaches a THG conversion efficiency of above 10^{-4}% and an ultrafast modulation depth of 1%, surpassing the response of the NbP bulk crystal in both cases. We attribute this improvement to the highly reduced volume of the thin film, which increases the interaction of the probing light with the topological surface states and minimizes linear absorption.

Altogether, our work demonstrates that the optical properties of epitaxially grown NbP thin films highly outperform their bulk counterpart, placing WSM thin films as promising candidates for on-chip all-optical switching and frequency conversion processes. Moreover, the NbP films pave the way for further control over the linear and NL optical response by enabling top-down fabrication techniques of WSM plasmonic nanodevices.[27–29]

2. Results and Discussion

NbP (001) thin films were grown by molecular-beam epitaxy along the [100]-direction of atomically flat MgO substrates.[30] To compensate for the MgO–NbP lattice mismatch, a Nb seed layer is grown with an in-plane rotation of 45° to the MgO substrate and phosphorized prior to the epitaxial growth of NbP (001). The layer growth is monitored in situ via reflection high-energy electron diffraction (RHEED) at all stages. **Figure 1**a shows the X-ray diffraction (XRD) pattern of the NbP thin film used in this work, which displays only the MgO substrate (002) and the NbP film (004) peak, demonstrating that the NbP film grows in a single crystalline fashion along the [001] direction, corresponding to the *c*-axis of the $I4_1md$, crystal structure of NbP. Streaky RHEED patterns along the in-plane directions are observed on this sample, indicating layer by layer growth, as exemplified in the inset of Figure 1a. Furthermore, the presence of X-ray reflectivity (XRR) oscillations (Figure 1b) confirms the structural long-range order and low roughness of the film. A numerical fit to the oscillations results in a thickness of 16 nm.

In order to obtain the dielectric function and therefore the optical constants $n(\omega)$, $k(\omega)$ of the NbP thin film, we performed spectral ellipsometry measurements. To maintain Kramers–Kronig consistency and extract the real and imaginary parts of the dielectric function $\varepsilon_1(\omega)$ and $\varepsilon_2(\omega)$, respectively, (Figure 1c) a numerical model was fitted to the ellipsometry data, considering Drude conductivity in the near infrared[31,32] and Lorentz curves in the visible regime. In contrast to common noble metals,[33] the real part $\varepsilon_1(\omega)$ is positive over the entire measured range and grows toward longer wavelengths. Only at the short wavelength limit ≈300 nm, the sign changes, corroborating theoretical calculations.[26] At the same time, the imaginary part $\varepsilon_2(\omega)$ is dominant and one order of magnitude larger than for most noble metals in the same spectral regime[33] and underlines the semimetallic character of NbP. It should be noted that an out-of-plane anisotropy found in the theoretical calculations was not observed here.[34] Most likely, the small thickness of the film prevents significant signs of the anisotropy to appear in the ellipsometry data.

Using the relations $\varepsilon_1 = n^2 - k^2$ and $\varepsilon_2 = 2nk$, the dielectric function can be converted to the refractive index $n(\omega)$ and the extinction coefficient $k(\omega)$, as shown in the Supporting Information. Remarkably, the refractive index stays nearly constant over the spectrum with slightly anomalous dispersion $\left(\frac{dn}{d\lambda} > 0\right)$, while the extinction coefficient shows a peak ≈350 nm and monotonically grows for increasing wavelengths. The values of the optical constants are further confirmed by transmission (orange) and reflection (blue) measurements that are shown in Figure 1d. The high refractive index combined with the strong linear absorption leads to a maximum transmission of only 30% and a reflection that stays below 50%. The measurement is modeled by finite-difference time-domain (FDTD) simulations that reproduce the achieved data with good agreement (see dashed lines in Figure 1d).

Next, the third-order NL optical response of the NbP film is further investigated. THG is generally described by the NL susceptibility $\chi^{(3)}(3\omega_0)$ and corresponds to the conversion of three incident photons of frequency ω_0 into a single higher energy photon with three times the original frequency $\omega_{\mathrm{THG}} = 3\omega_0$, or equivalently $\lambda_{\mathrm{THG}} = \frac{1}{3}\lambda_0$.[35–37] Consequently, **Figure 2**a shows respective THG spectra for fundamental wavelengths ranging from 1400–1950 nm, located at the respective third harmonic wavelengths. Furthermore, in a power dependent measurement in Figure 2b, the THG power clearly scales nonlinear with the excitation power. The inset shows a linear fit on a double-logarithmic scale, resulting in a slope close to three what proves the third-order nature of the observed signal. By directly measuring the THG power, we estimate a maximum efficiency of the NbP film to be $\eta_{\mathrm{THG}} \approx 10^{-4}$%, notably more than one order of magnitude larger than for the bulk crystal measured under

S. A. Maier
The Blackett Laboratory
Department of Physics
Imperial College London
London SW7 2AZ, UK

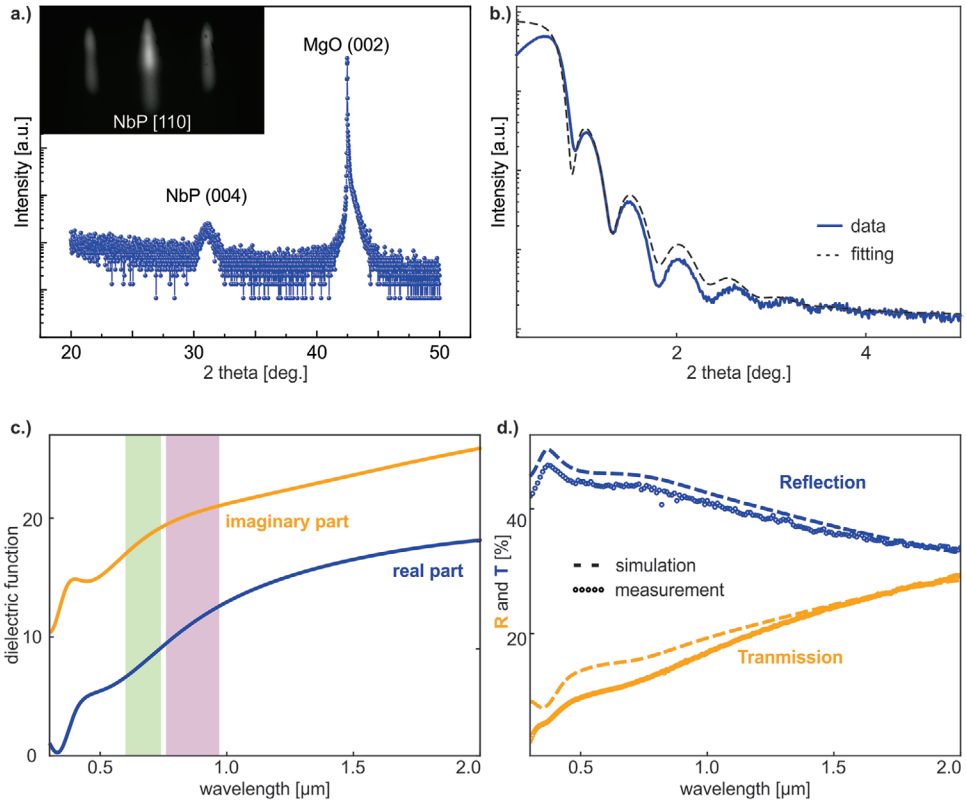

Figure 1. a) XRD pattern of the NbP film, with the (004) peak of NbP and the (002) peak of the MgO substrate indicated. Inset: In situ RHEED pattern of NbP, along the [110] direction. b) XRR measurement of the NbP film with the corresponding fit indicated by the dashed line. c) Real (blue) and imaginary (orange) part $\varepsilon_1(\omega)$ and $\varepsilon_2(\omega)$, respectively, of the dielectric function of NbP as determined by spectral ellipsometry. The shaded backgrounds indicate the spectral regime of the visible (green) and infrared (purple) beam of the pump–probe experiments. d) Transmission (orange) and reflection (blue) measurements of a NbP film at normal incidence with the respective results from FDTD simulations (dashed lines).

identical conditions (Supporting Information), three orders of magnitude larger than that of a germanium thin film, and only one to two orders of magnitude smaller compared to resonant germanium nanostructures.[38,39]

To understand the origin of the measured THG, we investigated the signal in dependence on the fundamental beam polarization, shown in Figure 2c,d, for 1400 and 1800 nm excitation wavelengths, respectively. Evidently, at 1400 nm the THG signal clearly peaks when the incident electric field is aligned with the *b*-axis of the crystal, while at 1800 nm it appears as almost polarization independent with a small dip at the *a*-axis. Interestingly, the bulk symmetry of the 4 mm symmetric NbP crystal can only generate THG with a fourfold polarization pattern.[35,36] However, at the surface of the material, the symmetry of the structure reduces to a C_{2v}-symmetry[40,41] that allows twofold polarization patterns, indicating that the observed THG is mostly generated by the surface states of NbP. A fitting of the nonzero tensor elements are shown by solid lines in Figure 2c,d, giving a good agreement with the experimental data (more details can be found in the Supporting Information). As it was recently shown that the surface states in identically fabricated NbP thin films are almost exclusively topological, due to a suppression of the trivial surfaces' states via atomic engineering,[30] we attribute the high observed efficiency to the topological surface states of NbP, in particular as they were shown the generate extremely high signal in other topological materials.[42] Figure 2e shows the relative THG efficiency over the excitation wavelength range from 1400–1950 nm with a clear peak ≈1800 nm. A comparison with calculations of the bandstructure of NbP[24,30] indicates that the small plateau in the conduction band, located at the Γ-point of the Brillouin zone is responsible for this resonance. Here the energy difference of valence and conduction bands equals the energy of the third-harmonic photon, enhancing the third-order NL process with two virtual electron states (for more details refer to Supporting Information). A comparison with the performance of the bulk NbP crystal shows that the THG has a comparable behavior (Supporting Information), but the resonant increase is not as large as for the thin film. This is not surprising since the latter is fully penetrated by the incident light, making it therefore possible to interact with the topological surface states at the top and the bottom of the film. Finally, it should be noted that due to the growth direction and the geometry of experimental setup, the NbP film is illuminated along the polar *c*-axis of the crystal where it appears centrosymmetric and consequently the previously reported efficient second-harmonic generation could not be observed.[18,43]

Next, we investigated the ultrafast optical response of the NbP films, using nondegenerate pump–probe spectroscopy with sub-10 fs pulses in the 600–1000 nm wavelength range.

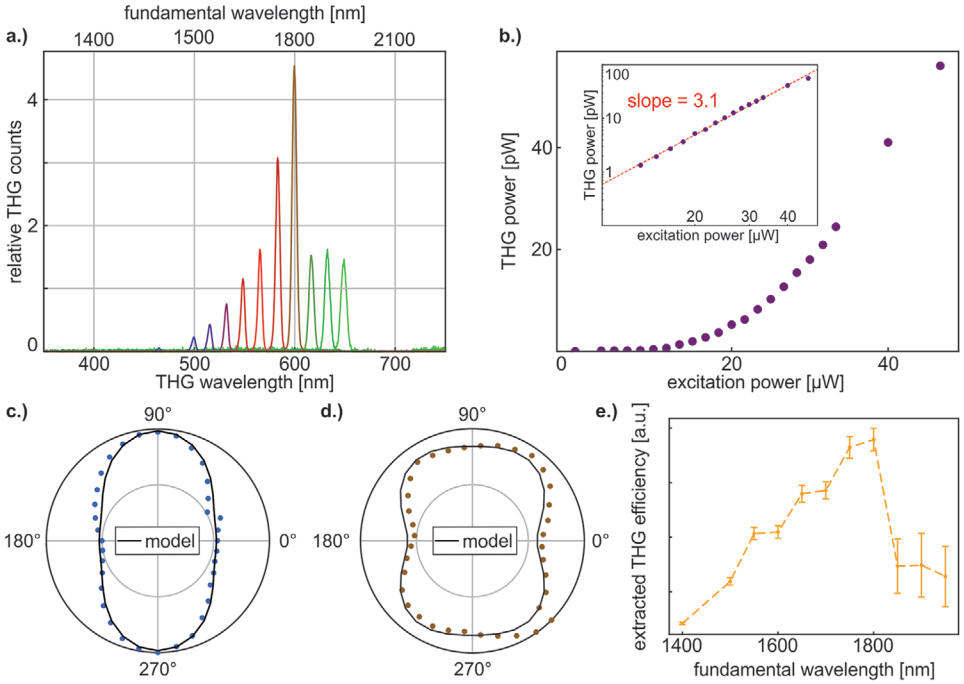

Figure 2. a) Relative THG spectra of the NbP thin film for different fundamental wavelengths ranging from 1400–1950 nm. b) Power dependence of the measured THG signal on the excitation power. The inset shows the same data on double logarithmic scale. A linear fit is shown by the dashed line, giving a slope of 3.1. c,d) Polarization dependence of the THG signal at 1400 nm (c) and 1800 nm (d). The solid line represents a fit of the nonlinear tensor elements to the data. e) Extracted relative THG efficiency for the NbP thin film at excitation wavelengths from 1400–1950 nm. The error bar is estimated from the uncertainty of the power measurement.

Dichroic beam splitters were used to divide the broadband beam into two beams of separate spectral components, the visible (600–750 nm) and infrared (750–1000 nm), which could act as pump and probe pulses interchangeably, while a motorized stage allowed us to tune the optical delay between them (more details can be found in the Experimental Section). The resulting differential reflectivity spectrum of the bulk (top graphs) and thin film (bottom graphs) are shown in **Figure 3**a–d for both pump/probe configurations. To understand the observed response, the electronic behavior in the Weyl cone is sketched in Figure 3e,f, following previous reports on ultrafast dynamics in WSMs[22,23,44] and graphene.[45,46] Starting from the intrinsic band structure, electrons absorb the incident pump photons and get promoted into the conduction band (Figure 3e). Via electron–electron (fast) and electron–phonon (slow) scattering, the excited electrons relax to lower energy states. As the density of states highly reduces toward the Weyl node, the relaxing electrons accumulate and delay the recombination process, leading to the formation of electron and hole seas above and below the Weyl node, respectively. Then, when the probe photons arrive, the optical response depends on whether their energies are high enough to excite electrons above the occupied states in the valence band (Figure 3f). Due to the lower energy of photons in the infrared beam, this is the case when probing with the visible beam and the arriving probe photons experience an increased absorption and thus a negative change of the reflectivity is observed (Figure 3a). This is not the case, however, when pumping the bulk crystal with the visible and probing with the lower energy infrared beam (Figure 3b). Here, photons in the high energy part of the probe beam (760–820 nm) are still absorbed by electrons and the change in reflectivity is negative but grows toward higher wavelengths. On the other hand, for wavelengths longer than 850 nm, the energy of the photons is no longer sufficient to excite valence electrons to available states and optical absorption is therefore Pauli blocked. As a consequence, the relative change of reflectivity becomes positive as the absorption of the materials gets reduced. In the intermediate regime ≈830 nm, a mixture of both situations is present that leads to a vanishing change in reflectivity. A better representation of the detected sign change is shown in **Figure 4**b, where the modulation at the temporal overlap (t = 0 fs) for each probe wavelength is displayed. Recent theoretical calculations of WSM's in ultrafast laser fields[47] predicted that the fast electron–electron scattering toward the Weyl node happens in the first 10 fs after the pump pulse arrives. Even though this is at the limit of the temporal resolution of the experimental setup, we attribute the sharp peak at the temporal overlap in Figure 3a,b to this ultrafast relaxation, visible in the single traces at selected 715 and 785 nm probe wavelengths in Figure 4a. A zoomed-in image of the first 500 fs can be found in the Supporting Information. After the initial ≈ 10 fs peak, a slower decay is observed, which can be fitted by an exponential decay function and can be fitted to the measured data resulting in 30, 97, and 97 fs for a probe wavelength of 715, 785, and 915 nm, respectively, as shown in Figure 4a. This is at the same scale as previously reported values for NbP crystals[22] or 2D graphene layers and comparable materials.[46,48–50] A very slow response with >100 ps characteristic decay time is found afterwards,

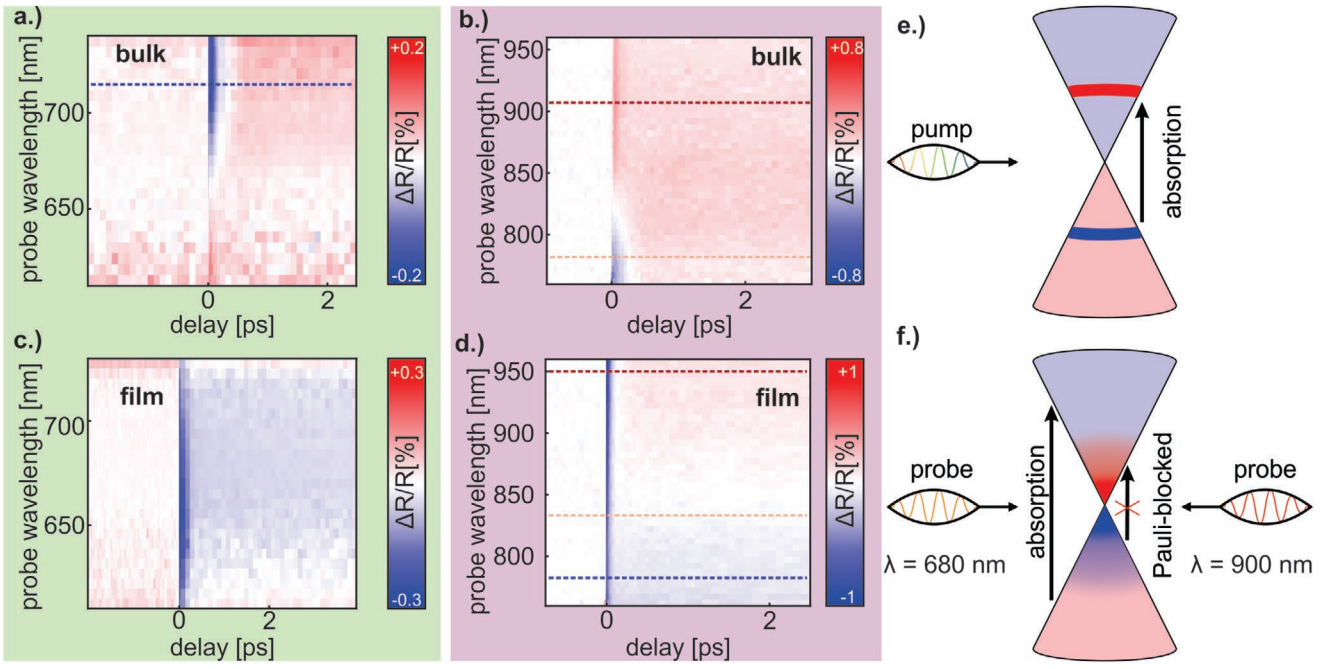

Figure 3. a–d) ltrafast pump–probe reflective spectroscopy of the bulk NbP crystal (a,b) and the thin film (c,d). The shaded background indicates the IR pulse (green, (a), (c)) or visible pulse (purple, (b), (c)) acting as pump beam, respectively. The dashed lines indicate the probe wavelength shown in Figure 4a,b. e,f) Sketch of the electron dynamics in the Weyl cone at the arrival of the pump pulse ($t = 0$ fs) (e) and at the arrival of the probe pulse ($t > 0$ fs) (f).

which is attributed to phonon–phonon scattering and is therefore present for all probe wavelengths. The measured change of reflectivity for the NbP thin film, shown in Figure 3c,d, markedly differs from the response of the bulk crystal. In particular at the temporal overlap, the sign of the modulation is negative for all probe wavelengths. When pumping with the infrared beam while probing with the visible beam (Figure 3c), the behavior of the film is comparable to that of the bulk crystal and therefore gives a response with the same sign and comparable magnitude. This can be attributed to the higher extinction coefficient in the pump wavelength regime and therefore ultrafast dynamics that are dominated by linear absorption, similar to the bulk case. On the other hand, when pumping with the visible beam (Figure 3d), the shape of the modulation differs fundamentally. The maximum change of reflectivity has a constantly negative sign and lacks a significant spectral dependence on the probe wavelength and completely decays within 100 fs. Moreover, a power dependence of the modulation depth (Supporting Information) shows a clear linear scaling with increasing pump intensity. This indicates that the change in reflectivity is caused by a pump-induced change of the refractive index that can be described by $\tilde{n}(I_{\text{pump}}) = n_0 + n' I_{\text{pump}}$.[51] Here, n_0 indicates the complex linear refractive index while the nonlinear coefficient n'encompasses the effective nonlinear refractive index n_2 and the two-photon absorption coefficient β. The first corresponds to a change of the real part of the refractive index, while the latter represents a change of the imaginary part. Even though both processes are third-order nonlinear effects, the high peak electric field strengths and the high third-order susceptibility of NbP as revealed by the pronounced THG efficiency lead to the observed modulation. Simulations shown in Figure S5, Supporting Information, show with good agreement that the observed modulation corresponds to a homogeneous change of the complex refractive index by roughly 5%. For three representative probe wavelengths, single temporal traces are shown in Figure 4c, including exponential decay functions convoluted with the instrument responds function (IRF) of the system that were fitted to the measured data. The resulting time constants of 32, 33, and 55 fs for 785, 835, and 950 nm probe wavelengths, respectively, evidence the ultrafast nature of the measured modulation. The fact that these values are in the same range as reported for all-optical modulations in dielectric materials[51–53] further corroborates the nonlinear nature of the observed signal.

We explain the difference between the electronically dominated dynamics in the bulk crystal and the nonlinear optical modulation in the thin film with the fact that even though both have the same nonlinear properties, linear absorption in the bulk crystal is too dominant and therefore limits direct pump and probe pulse interactions necessary for all-optical modulations. Comparing the maximum change in reflectivity of −0.8% for the NbP film shows this is in the same range as reported values for 2D perovskite nanosheets[54] and amorphous gallium phosphide thin films.[53] The temporal traces in Figure 4c reveal another interesting feature of the thin film. At long delay times, a negative to positive sign change is found when increasing the probe wavelength, as noticeable in Figure 4d at a fixed 2 ps delay time. The modulation is negative for wavelengths shorter than 850 nm and becomes positive for longer wavelengths, while completely vanishing in between. As the wavelength of the sign change is close to the corresponding value for the bulk crystal at the temporal overlap (Figure 4b),

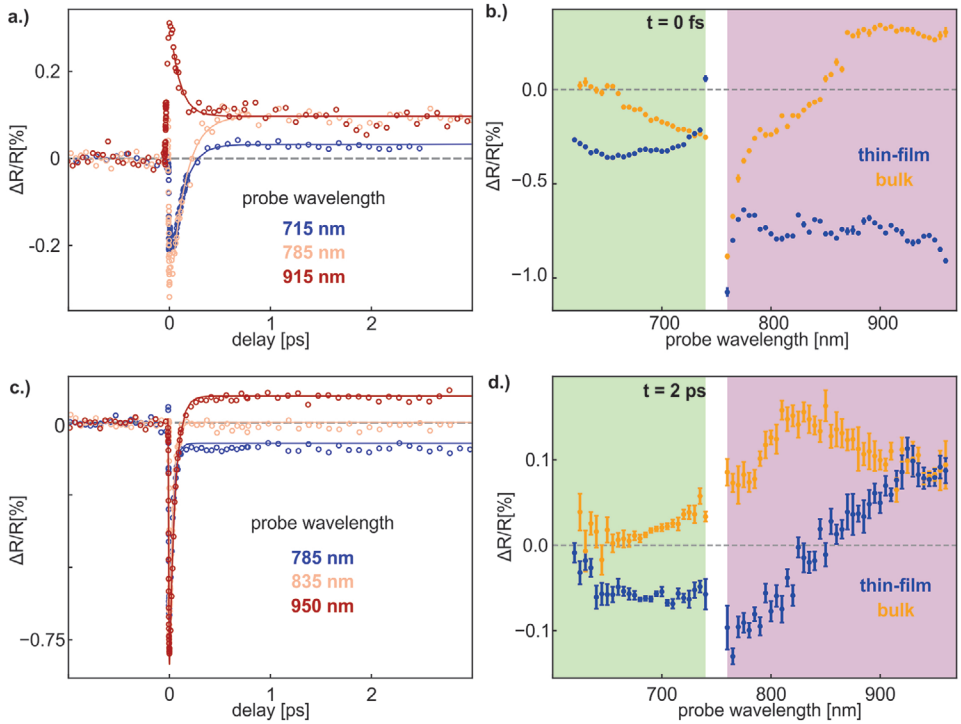

Figure 4. a) Single time traces for the bulk NbP crystal at 715 (blue), 785 (beige), and 915 nm (dark red) probe wavelengths, respectively. The solid lines represent a fit of an exponential decay function to the slow decaying part of the signal. b) Maximum relative change of reflectivity at the overlap of pump and probe pulse (t = 0 fs) for the NbP thin film (blue) and bulk crystal (orange). c) Time traces of the NbP thin film at 785 (blue), 835 (beige), and 950 nm (dark red) probe wavelengths, respectively. The solid lines represent fittings of an exponential decay function, convoluted with the instrument response function of the system. d) Relative change of reflectivity after the ultrafast relaxation (t = 2 ps) for the NbP thin film (blue) and bulk crystal (orange). The shaded backgrounds in (b) or (d) indicate the visible (green) or infrared (purple) beam acting as the pump, respectively.

we attribute this slow response again to the carrier dynamics in the Weyl cone. Since the pump beam travels through the entire thin film (which consists of only 15–20 unit cells[24]), the number of available states around the illuminated spot is significantly reduced compared to the bulk crystal. Therefore, the relaxation process of the electrons is further delayed and the electron accumulation above the Weyl node is still visible after 2 ps. This indicates that when probing with a wavelength of 850 nm, the beam exhibits a strong optical modulation from the pump beam and the nature of the Weyl cone prevents linear absorption effects. Therefore, the ultrafast signal completely decays in less than 100 fs, lacking a slow residual component. This suggests that further engineering would allow (nano) devices based on NbP with all-optical switching bandwidths of up to 10 THz, outperforming other systems such as indium tin oxide (ITO) at the epsilon near-zero wavelength by almost one order of magnitude.[55–57] Even for the other probe wavelength in the infrared pulse, the ratio between the peak ultrafast modulation and the slow relaxing tail is large enough to obtain clear on- and off-states, emphasizing NbP as a promising material for all optical switching. It should further be noted that the slow response far from the sign change region appear temporally almost constant, even for longer timescale measurements (see Supporting Information). This indicates long electronic lifetimes in the nanosecond time range and could be a promising property for light harvesting or detection applications.

3. Conclusion

We have investigated the linear and third-order NL optical properties of a NbP thin film with a bulk single crystal as reference. Even though the imaginary part of the linear dielectric function was measured to be dominant over the studied spectral range, we detected strong THG from the thin film, exceeding the efficiency of the bulk material by more than a factor of 12. Moreover, a clear contrast in the response of the two samples was found through ultrafast differential reflectivity measurements. We observed the electron dynamics change from an optical absorption dominated response in the bulk crystal to an optical NL regime in the thin film, enabling sub-100 fs reflectivity modulations at wavelengths close to 850 nm. Our work strengthens the potential of WSM thin films as promising material platforms with possible applications in the fields of nanophotonics, including all-optical switching, efficient frequency conversion, and light harvesting.

4. Experimental Section

Sample Fabrication: The NbP thin films were grown by molecular-beam epitaxy in a custom made ultra-high vacuum chamber ($p_{base} = 1 \times 10^{-10}$ mbar), using electron-beam heating of a niobium rod and parallel thermalization of a gallium phosphide compound effusion cell to get the phosphide species. A cross-beam mass spectrometer was used to calibrate the atomic fluxes, while the substrate temperature was

controlled by radiation heating. More details on the fabrication of the NbP films can be found published elsewhere.[24]

The bulk NbP crystals were grown via chemical transport reaction with iodine as transport agent and a temperature gradient from 850 °C at the source to 950 °C at the sink. Beforehand, a polycrystalline powder of NbP was synthesized from niobium and red phosphorus via direct chemical reaction at 800 °C. More detail on the fabrication and characterization of the single NbP crystals can be found elsewhere.[12]

Sample Characterization: XRD and XRR measurements were performed with a commercial diffractometer from Bruker, using Cu Kα radiation. In situ RHEED monitoring was performed with a 15 kV electron beam. Ellipsometry measurements were done with a variable-angle spectroscopic ellipsometry (VASE) instrument from J. A. Woollam over the visible to near-infrared spectral range (300–2000 nm). The numerical fitting was performed with the WVASE software from the same company, using a model of multiple Lorentz-like peak functions and a Drude dispersion model in the low energy regime. The same tool was used to perform the linear transmission and reflection measurements.

THG Experiments: The used laser system comprised a Yb:KGW Pharos 1030 nm pump laser with a repetition rate of 200 kHz that pumped a collinear optical parametric amplifier (OPA) Orpheus-HP (both by Light Conversion Ltd.). The output of the OPA could be freely tuned from 300 nm and 3 μm with an approximate pulse duration of 180 fs that was then sent to a microscope with a 100x/ numerical aperture (NA) = 0.9 objective that focused the beam on the sample. The generated THG light was then collected by the same objective (reflection) or by a NA = 0.6 objective (transmission) and subsequently sent to a spectrometer or a calibrated silicon powermeter (Newport). Due to spectral limitations of the experimental setup, reflection measurements could only be performed from 1500–1650 nm. For polarization dependent measurements, a waveplate ($\lambda/2$) was placed in the beam path before the microscope.

Pump–Probe Experiments: The same laser system as for the THG experiments was used to pump a 5 mm-thick sapphire plate at 1120 nm with an average power of 600 mW to generate 3 mW of supercontinuum (SC) light. A multiphoton intrapulse interference phase scan device (MIIPSBox640-P by Biophotonic Solutions Inc.) was used to temporally compress the pulse to below 10 fs full-width at half maximum at the sample position. The measured autocorrelation of the two pulses are shown in the Supporting Information. A motorized delay line in combination with dichroic beam splitters allowed the authors to divide the spectrum in two 600–750 and 750–1000 nm independent beams with a controllable temporal offset and below 1 fs accuracy. To minimize dispersion effects, low group velocity dispersion mirrors and a dispersion-free reverse Cassegrain objective with NA = 0.5 were used to direct and focus the beams onto the sample. The experiments were conducted with a 5:1 (pump:probe) power ratio, using average powers of 10 and 2 µW for pump and probe pulses, respectively. The collected signal was then sent to a spectrograph coupled to a low-noise photodiode (FEMTO). Lock-in detection was used by modulating the pump beam with a mechanical chopper operating at frequencies below 1 kHz. The instrument response function of the system is described by a Gaussian function with a full-width half-maximum of 10 fs (Supporting Information), that approximates the convolution of pump and probe pulses. More details on the experimental pump–probe setup can be found published elsewhere.[51]

Numerical Simulations: The numerical simulations were performed with the commercially available software Lumerical FDTD. Perfectly matched layer and periodic boundary conditions were used to mimic an infinitely extended sample surrounded by infinite space. A broadband plane wave source at normal incidence illuminated the sample. Field monitors above and below the film were used to collect the data for reflection and transmission calculations, respectively. The measured dielectric function of the MgO substrate and the NbP film were implemented as material data for the simulations.

Supporting Information

Supporting Information is available from the Wiley Online Library or from the author.

Acknowledgements

This work was funded by the Deutsche Forschungsgemeinschaft (DFG, German Research Foundation) under Germany's Excellence Strategy, EXC 2089/1-390776260, and the Bavarian programme Solar Energies Go Hybrid (SolTech). The authors also acknowledge the support of the Center for NanoScience (CeNS). S.A.M. additionally acknowledges the EPSRC Reactive Plasmonics Programme (EP/M013812/1) and the Lee-Lucas Chair in Physics. G.G acknowledges support by PICT grant No. 2019-01886. Y.L. acknowledges the Natural Science Foundation of Guandong Province (2019A1515111136) as well as the European Union's Framework Programme for Research and Innovation Horizon 2020 (2014–2020) under the Marie Skłodowska-Curie Grant Agreement No. 754388 (LMU Research Fellows) and from LMUexcellent as part of LMU Munich's funding as University of Excellence within the framework of the German Excellence Strategy. C.S. and C.F. acknowledge the European Research Council (ERC) Advanced Grant No. 742068 ("TOPMAT").

Open access funding enabled and organized by Projekt DEAL.

Conflict of Interest

The authors declare no conflict of interest.

Data Availability Statement

The data that support the findings of this study are available from the corresponding author upon reasonable request.

Keywords

nonlinear optics, pump–probe spectroscopy, thin films, ultrafast optics, Weyl semimetals

Received: August 26, 2021
Revised: February 11, 2022
Published online: March 3, 2022

[1] S.-Y. Xu, I. Belopolski, N. Alidoust, M. Neupane, G. Bian, C. Zhang, R. Sankar, G. Chang, Z. Yuan, C.-C. Lee, S.-M. Huang, H. Zheng, J. Ma, D. S. Sanchez, B. Wang, A. Bansil, F. Chou, P. P. Shibayev, H. Lin, S. Jia, M. Z. Hasan, *Science* **2015**, *349*, 613.
[2] N. P. Armitage, E. J. Mele, A. Vishwanath, *Rev. Mod. Phys.* **2018**, *90*, 015001.
[3] H. Weyl, *Proc. Natl. Acad. Sci. USA* **1929**, *15*, 323.
[4] S.-M. Huang, S.-Y. Xu, I. Belopolski, C.-C. Lee, G. Chang, B. Wang, N. Alidoust, G. Bian, M. Neupane, C. Zhang, S. Jia, A. Bansil, H. Lin, M. Z. Hasan, *Nat. Commun.* **2015**, *6*, 7373.
[5] I. Belopolski, S.-Y. Xu, D. S. Sanchez, G. Chang, C. Guo, M. Neupane, H. Zheng, C.-C. Lee, S.-M. Huang, G. Bian, N. Alidoust, T.-R. Chang, B. Wang, X. Zhang, A. Bansil, H.-T. Jeng, H. Lin, S. Jia, M. Z. Hasan, *Phys. Rev. Lett.* **2016**, *116*, 066802.
[6] S. Jia, S.-Y. Xu, M. Z. Hasan, *Nat. Mater.* **2016**, *15*, 1140.
[7] N. Nagaosa, T. Morimoto, Y. Tokura, *Nat. Rev. Mater.* **2020**, *5*, 621.

[8] M. R. van Delft, S. Pezzini, M. König, P. Tinnemans, N. E. Hussey, S. Wiedmann, arXiv: 1808.09702, **2018**.
[9] R. Nandkishore, *Phys. Rev. B* **2016**, *93*, 020506.
[10] M. D. Bachmann, N. Nair, F. Flicker, R. Ilan, T. Meng, N. J. Ghimire, E. D. Bauer, F. Ronning, J. G. Analytis, P. J. W. Moll, *Sci. Adv.* **2017**, *3*, e1602983.
[11] B. Yan, C. Felser, *Annu. Rev. Condens. Matter Phys.* **2017**, *8*, 337.
[12] C. Shekhar, A. K. Nayak, Y. Sun, M. Schmidt, M. Nicklas, I. Leermakers, U. Zeitler, Y. Skourski, J. Wosnitza, Z. Liu, Y. Chen, W. Schnelle, H. Borrmann, Y. Grin, C. Felser, B. Yan, *Nat. Phys.* **2015**, *11*, 645.
[13] H. Reichlova, R. Schlitz, S. Beckert, P. Swekis, A. Markou, Y.-C. Chen, D. Kriegner, S. Fabretti, G. Hyeon Park, A. Niemann, S. Sudheendra, A. Thomas, K. Nielsch, C. Felser, S. T. B. Goennenwein, *Appl. Phys. Lett.* **2018**, *113*, 212405.
[14] J. Yan, C. Ma, P. Liu, C. Wang, G. Yang, *Nano Lett.* **2017**, *17*, 4793.
[15] N. Xu, H. M. Weng, B. Q. Lv, C. E. Matt, J. Park, F. Bisti, V. N. Strocov, D. Gawryluk, E. Pomjakushina, K. Conder, N. C. Plumb, M. Radovic, G. Autès, O. V. Yazyev, Z. Fang, X. Dai, T. Qian, J. Mesot, H. Ding, M. Shi, *Nat. Commun.* **2016**, *7*, 11006.
[16] H. B. Nielsen, M. Ninomiya, *Phys. Lett. B* **1983**, *130*, 389.
[17] A. A. Burkov, *J. Phys.: Condens. Matter* **2015**, *27*, 113201.
[18] L. Wu, S. Patankar, T. Morimoto, N. L. Nair, E. Thewalt, A. Little, J. G. Analytis, J. E. Moore, J. Orenstein, *Nat. Phys.* **2017**, *13*, 350.
[19] J. Ma, Q. Gu, Y. Liu, J. Lai, P. Yu, X. Zhuo, Z. Liu, J.-H. Chen, J. Feng, D. Sun, *Nat. Mater.* **2019**, *18*, 476.
[20] G. B. Osterhoudt, L. K. Diebel, M. J. Gray, X. Yang, J. Stanco, X. Huang, B. Shen, N. Ni, P. J. W. Moll, Y. Ran, K. S. Burch, *Nat. Mater.* **2019**, *18*, 471.
[21] C. R. Rajamathi, U. Gupta, N. Kumar, H. Yang, Y. Sun, V. Süß, C. Shekhar, M. Schmidt, H. Blumtritt, P. Werner, B. Yan, S. Parkin, C. Felser, C. N. R. Rao, *Adv. Mater.* **2017**, *29*, 1606202.
[22] C. P. Weber, B. S. Berggren, M. G. Masten, T. C. Ogloza, S. Deckoff-Jones, J. Madéo, M. K. L. Man, K. M. Dani, L. Zhao, G. Chen, J. Liu, Z. Mao, L. M. Schoop, B. V. Lotsch, S. S. P. Parkin, M. Ali, *J. Appl. Phys.* **2017**, *122*, 223102.
[23] C. P. Weber, L. M. Schoop, S. S. P. Parkin, R. C. Newby, A. Nateprov, B. Lotsch, B. M. K. Mariserla, J. M. Kim, K. M. Dani, H. A. Bechtel, E. Arushanov, M. Ali, *Appl. Phys. Lett.* **2018**, *113*, 221906.
[24] A. Bedoya-Pinto, A. K. Pandeya, D. Liu, H. Deniz, K. Chang, H. Tan, H. Han, J. Jena, I. Kostanovskiy, S. S. P. Parkin, *ACS Nano* **2020**, *14*, 4405.
[25] S.-C. Wu, Y. Sun, C. Felser, B. Yan, *Phys. Rev. B* **2017**, *96*, 165113.
[26] D. Grassano, O. Pulci, A. Mosca Conte, F. Bechstedt, *Sci. Rep.* **2018**, *8*, 3534.
[27] E. Ozbay, *Science* **2012**, *189*, 189.
[28] A. D. Boardman, A. V. Zayats, *Handb. Surf. Sci.* **2014**, *4*, 329.
[29] S. A. Maier, *Plasmonics: Fundamentals and Applications. Plasmonics: Fundamentals and Applications*, Pringer Science+Business Media LLC, New York **2007**.
[30] A. Bedoya-Pinto, D. Liu, H. Tan, A. K. Pandeya, K. Chang, J. Zhang, S. S. P. Parkin, *Adv. Mater.* **2021**, *33*, 2008634.
[31] S.-I. Kimura, H. Yokoyama, H. Watanabe, J. Sichelschmidt, V. Süß, M. Schmidt, C. Felser, *Phys. Rev. B* **2017**, *96*, 075119.
[32] B. Xu, Y. M. Dai, L. X. Zhao, K. Wang, R. Yang, W. Zhang, J. Y. Liu, H. Xiao, G. F. Chen, A. J. Taylor, D. A. Yarotski, R. P. Prasankumar, X. G. Qiu, *Phys. Rev. B* **2016**, *93*, 121110.
[33] E. D. Palik, in *Handbook of Optical Constants of Solids iii*, Elsevier, Amsterdam **1998**.
[34] J. Buckeridge, D. Jevdokimovs, C. R. A. Catlow, A. A. Sokol, *Phys. Rev. B* **2016**, *93*, 125205.
[35] R. W. Boyd, *Nonlinear Optics*, Elsevir Academic Press, Amsterdam, The Netherlands **2008**. pp. 1–67.
[36] D. C. Hanna, *The Principles of Nonlinear Optics*, Wiley, New York **1985**.
[37] T. Zhang, K. J. A. Ooi, W. Chen, L. K. Ang, Y. Sin Ang, *Opt. Express* **2019**, *27*, 38270.
[38] G. Grinblat, Y. Li, M. P. Nielsen, R. F. Oulton, S. A. Maier, *Nano Lett.* **2016**, *16*, 4635.
[39] G. Grinblat, Y. Li, M. P. Nielsen, R. F. Oulton, S. A. Maier, *ACS Nano* **2017**, *11*, 953.
[40] S. Chi, Z. Li, H. Yu, G. Wang, S. Wang, H. Zhang, J. Wang, *Ann. Phys. (Berlin)* **2017**, *529*, 1600359.
[41] Y. Sun, S.-C. Wu, B. Yan, *Phys. Rev. B: Condens. Matter Mater. Phys.* **2015**, *92*, 115428.
[42] S. Chi, F. Liang, H. Chen, W. Tian, H. Zhang, H. Yu, G. Wang, Z. Lin, J. Hu, H. Zhang, *Adv. Mater.* **2020**, *32*, 1904498.
[43] S. Patankar, L. Wu, B. Lu, M. Rai, J. D. Tran, T. Morimoto, D. E. Parker, A. G. Grushin, N. L. Nair, J. G. Analytis, J. E. Moore, J. Orenstein, D. H. Torchinsky, *Phys. Rev. B* **2018**, *98*, 165113.
[44] R. J. Kirby, A. Ferrenti, C. Weinberg, S. Klemenz, M. Oudah, S. Lei, C. P. Weber, D. Fausti, G. D. Scholes, L. M. Schoop, *J. Phys. Chem. Lett.* **2020**, *11*, 6105.
[45] M. Baudisch, A. Marini, J. D. Cox, T. Zhu, F. Silva, S. Teichmann, M. Massicotte, F. Koppens, L. S. Levitov, F. J. García De Abajo, J. Biegert, *Nat. Commun.* **2018**, *9*, 1018.
[46] D. Brida, A. Tomadin, C. Manzoni, Y. J. Kim, A. Lombardo, S. Milana, R. R. Nair, K. S. Novoselov, A. C. Ferrari, G. Cerullo, M. Polini, *Nat. Commun.* **2013**, *4*, 1987.
[47] F. Nematollahi, S. A. Oliaei Motlagh, V. Apalkov, M. I. Stockman, *Phys. Rev. B* **2019**, *99*, 245409.
[48] C. Trovatello, F. Katsch, N. J. Borys, M. Selig, K. Yao, R. Borrego-Varillas, F. Scotognella, I. Kriegel, A. Yan, A. Zettl, P. J. Schuck, A. Knorr, G. Cerullo, S. D. Conte, *Nat. Commun.* **2020**, *11*, 5277.
[49] S. Ahmed, X. Jiang, F. Zhang, H. Zhang, *J. Phys. D: Appl. Phys.* **2020**, *53*, 473001.
[50] K. Oum, T. Lenzer, M. Scholz, D. Y. Jung, O. Sul, B. J. Cho, J. Lange, A. Müller, *J. Phys. Chem. C* **2014**, *118*, 6454.
[51] G. Grinblat, M. P. Nielsen, P. Dichtl, Y. Li, R. F. Oulton, S. A. Maier, *Sci. Adv.* **2019**, *5*, eaaw3262.
[52] G. Grinblat, H. Zhang, M. P. Nielsen, L. Krivitsky, R. Berté, Y. Li, B. Tilmann, E. Cortés, R. F. Oulton, A. I. Kuznetsov, S. A. Maier, *Sci. Adv.* **2020**, *6*, eabb3123.
[53] B. Tilmann, G. Grinblat, R. Berté, M. Özcan, V. F. Kunzelmann, B. Nickel, I. D. Sharp, E. Cortés, S. A. Maier, Y. Li, *Nanoscale Horiz.* **2020**, *5*, 1500.
[54] G. Grinblat, I. Abdelwahab, M. P. Nielsen, P. Dichtl, K. Leng, R. F. Oulton, K. P. Loh, S. A. Maier, *ACS Nano* **2019**, *13*, 9504.
[55] M. Z. Alam, S. A. Schulz, J. Upham, I. De Leon, R. W. Boyd, *Nat. Photonics* **2018**, *12*, 79.
[56] M. Z. Alam, I. De Leon, R. W. Boyd, *Science* **2016**, *352*, 795.
[57] P. Guo, R. D. Schaller, J. B. Ketterson, R. P. H. Chang, *Nat. Photonics* **2016**, *10*, 267.